MAVEN: An Algorithm for Multi-Parametric Automated Segmentation of Brain Veins From Gradient Echo Acquisitions

Serena Monti,* Sirio Cocozza, Pasquale Borrelli, Sina Straub, Mark E. Ladd, Marco Salvatore, Enrico Tedeschi, and Giuseppe Palma

***Abstract*— Cerebral vein analysis provides a chance to study, from an unusual viewpoint, an entire class of brain diseases, including neurodegenerative disorders and traumatic brain injuries. Manual segmentation approaches can be used to assess vascular anatomy, but they are observer-dependent and time-consuming; therefore, automated approaches are desirable, as they also improve reproducibility. In this paper, a new, fully automated algorithm, based on structural, morphological, and relaxometric information, is proposed to segment the entire cerebral venous system from MR images. The algorithm for multi-parametric automated segmentation of brain VEiNs (MAVEN) is based on a combined investigation of multi-parametric information that allows for rejection of false positives and detection of thin vessels. The method is tested on gradient echo brain data sets acquired at 1.5, 3, and 7 T. It is compared to previous methods against manual segmentation, and its inter-scan reproducibility is assessed. The achieved accuracy and reproducibility are good, meaning that MAVEN outperforms previous methods on both quantitative and qualitative analyses. It is usable at all the field strengths explored, showing comparable accuracy scores, with no need for algorithm parameter adjustments, and thus, it is a promising candidate for the characterization of the venous tree topology.**

***Index Terms*— Brain veins, vesselness, segmentation, MRI.**

I. Introduction

THE intracranial venous tree can be proficiently visualized by Susceptibility Weighted Imaging (SWI) [1]. This technique allows for the depiction of the anatomy of deep cerebral veins and their abnormalities, which occur in different brain pathologies, such as isolated cortical vein thrombosis [2] and acute brain injury [3], or may be a feature of different neurological conditions [4], ranging from neuroinflammatory diseases [5], [6] to idiopathic intracranial hypertension [7]. Assessing vascular anatomy is then crucial, since accurate segmentation and extraction of the cerebral venous system may help quantitative clinical research, as demonstrated in diseases primarily affecting the venous system [8], [9], but also in pathologies (such as Alzheimer's disease [10], normal pressure hydrocephalus [11], leukoaraiosis [12], [13], multiple sclerosis [14]–[16], traumatic brain injury [17], and perinatal encephalopathy [18]) in which deep brain veins are secondarily involved and may thus represent an index of pathophysiologic alterations. Moreover, accurate vessel tracking is obviously important in clinical situations where deep brain percutaneous intervention is planned [19].

Unfortunately, manual segmentation of the vascular tree is not possible in reasonable times: a whole brain time-of-flight Magnetic Resonance (MR) angiography can take up to 8 weeks to be segmented manually [20]. Such a task is even more daunting and time-consuming in a denser SWI dataset, also due to the narrowness of the structures and the complexity of the patterns to be tracked both in-plane and through-plane. Hence, semi-automated or automated approaches are actively sought, as they also improve the reproducibility of the results.

Several automated or semi-automated methods for vessel segmentation are described in the literature [21]. They can be divided into scale-space analysis, statistical methods and deformable models. Currently, the segmentation approaches most often and successfully applied to SWI are based on scale-space analysis [22]–[24] or statistical models [17], [25]. Each of them has its own limitations and is prone to detect false positives or to under-segment some structures [25]. In this context, combinations of scale-space approaches with statistical methods [26], [27] or deformable models [28]–[30] have been proposed, but, mainly due to the high variability of the susceptibility weighting at different magnetic field strengths (B_0), they have only been assessed at a fixed B_0 value. However, a feasibility study on a wider range of field strengths could be beneficial [30]. Another common drawback of these methods is that, according to the targeted application, they are usually more robust in some brain regions than in others.

This work presents an algorithm for Multi-parametric Automated VEiN segmentation (MAVEN) that is, to the best of

Manuscript received October 22, 2016; revised December 21, 2016; accepted December 22, 2016. Date of publication February 20, 2017; date of current version April 30, 2017. This work was supported by the Italian Minister of Health under Grant RRC-2015-2360454. *Asterisk indicates corresponding author.*

*S. Monti is with IRCCS SDN, 80143 Naples, Italy, and also with the Department of Electronic, Information and Bioengineering, Politecnico di Milano, 20133 Milan, Italy (e-mail: serena.monti@polimi.it).

S. Cocozza and E. Tedeschi are with the Department of Advanced Biomedical Sciences, University Federico II, 80131 Naples, Italy.

P. Borrelli and M. Salvatore are with IRCCS SDN, 80143 Naples, Italy.

S. Straub and M. E. Ladd are with the Department of Medical Physics in Radiology, German Cancer Research Center, 69120 Heidelberg, Germany.

G. Palma is with the Institute of Biostructure and Bioimaging, National Research Council, 80145 Naples, Italy.

Digital Object Identifier 10.1109/TMI.2016.2645286

our knowledge, the first fully automated segmentation tool of the entire cerebral venous system implementing at once several independent criteria (structural, morphological and relaxometric information) of vein characterization to enhance classification accuracy [31]. The aim of this study is to obtain a method usable on a wide spectrum of B_0 and capable of providing highly reproducible segmentation results.

In the following, we present the description of the developed algorithm (§II) and the experimental methodology to validate MAVEN performance (§III). After the analysis of segmentation results (§IV), the findings of this work are discussed and conclusions are drawn (§V).

II. Methods

The segmentation of cerebral veins is a labeling problem whose objective is to obtain a logical vein mask S classifying each voxel $\vec{x}$ as belonging ($S(\vec{x}) = \text{True}$) or not ($S(\vec{x}) = \text{False}$) to a vein, on the basis of some hypotheses about vessel/other-tissue statistical distribution in the observed data.

Our method exploits three different sources of information to devise as many independent criteria of vein characterization:

- structural information, carried by SWI;
- morphological information, described by Vesselness maps V (*i.e.* a measure of the probability that the signal in the neighborhood of a given point is compatible with a vessel-like structure; it is computed by the Vessel Enhancing Diffusion filter from SWI and Quantitative Susceptibility Mapping – QSM – [17] as in Appendix A);
- relaxometric information, contained in R_2^*-maps (see Appendix B for details).

In this multi-parametric approach, vein voxels are characterized by hypo-intensity in SWI and have high Vesselness and R_2^* values compared to other tissues.

MAVEN represents a largely rethought version of the statistical method described in [17], originally meant to be applied only on the SWI images.

A sketch of the algorithm flowchart is shown in Fig. 1, and the rationale behind it is briefly described below.

An excellent starting point is represented by a global thresholding on a combination of the Vesselness maps derived from the SWI and QSM: the former provides a good sensitivity to small vessels, while the latter correctly handles the contrast of large veins that are usually washed out in SWI. A useful expedient to make the Vesselness function less sensitive to tubular-like artifacts due to non-local field inhomogeneities consists in a preliminary regularization according to the estimated local field gradient. This step, however, excludes the tiniest veins, which are broadened and whose Vesselness values are typically lowered by the diffusion steps to the same order of magnitude of CSF-filled sulci (which are hypo-intense in SWI due to their low R_1 value). Therefore, it is necessary to refine the vein mask by adding voxels that satisfy a condition based on a lower threshold applied on SWI-Vesselness, properly combined with two further thresholds on SWI and R_2^*. The former is aimed to enforce vessel extension within the actual anatomical details, the latter to properly exclude CSF structures that match Vesselness- and SWI-based criteria.

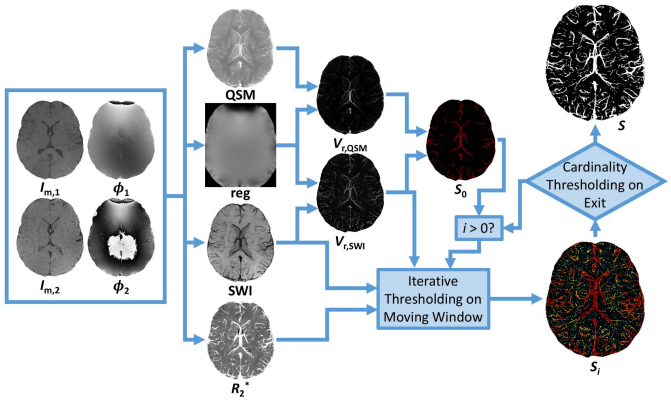

Fig. 1. Schematic flowchart of the MAVEN algorithm. From a double-echo gradient echo acquisition, a pair of 3D magnitude $I_{m,i}$ and phase ϕ_i images is obtained at each echo time $T_{E,i}$, $i \in \{1, 2\}$. They are used to compute QSM, SWI, R_2^*-map (Appendix V) and a B_0 regularization function (§II-A). The regularized Vesselness functions (Appendix V) from QSM and SWI are used to obtain an initial condition S_0 (§II-B). Then, the current estimate of the asymptotic vein mask is iteratively computed by the moving window filter that uses as input SWI, Vesselness from SWI, R_2^*-maps and the estimate from the previous step (§II-C). When the exit condition is met, a cardinality thresholding is applied to obtain the final MAVEN segmentation.

This combined condition is better applied on a local moving window, since at least one of the involved contrasts (namely, the SWI) depends on the coil sensitivity, which usually shows long wavelength oscillations that may invalidate the results of a global thresholding. In this process, the thresholds are based on the statistical moments of the three maps computed in the moving window. Therefore, the exclusion of voxels previously marked as vein in the computation of mean and standard deviation may allow an iterative approach to identify also small vessels, which typically have less marked contrast due to partial volume effect. In addition, once the risk of having a local signal distribution skewed by the presence of a large vessel has been prevented, a smaller moving window can be used in the next steps of the iteration, in order to enhance the sensitivity to local information.

In the following, a solution to the problem of regularizing the Vesselness in regions of highly inhomogeneous B_0 field is proposed (§II-A), and a detailed description of the setup of MAVEN initial condition (§II-B) and subsequent iterations (§II-C) is provided.

A. Vesselness Regularization

Regions with severe non-local field inhomogeneities (SNLFI), such as the temporo-basal regions (above the roofs of the petrous bones), the fronto-basal region on the midline (*i.e.* near the air/bone interface of the skull base) and the interhemispheric fissure, are troublesome for the segmentation algorithm. Indeed, an imperfect shim or high susceptibility contrast aside these peripheral parenchyma regions induce SNLFI that cause both unwanted gradients in phase images and intra-voxel decay of isochromat coherence (*i.e.* signal loss) in magnitude images. Therefore, a considerable amount of parenchyma voxels may resemble vein signal intensity in SWI, Vesselness and R_2^* maps.

Consequently, the algorithm needs to be tuned up in order to be more selective in the regions of field inhomogeneities not related to parenchyma properties. This goal is accomplished by regularizing overestimated Vesselness maps V with a function that takes into account the spatial variation of the magnetic field as estimated from the phase images, so that vessel-like artifacts are appropriately damped.

In order to assess the SNLFI, the associated residual phase variation (RPV) is first computed as:

$$\mathrm{RPV}(\vec{x}) = \left(\phi(\vec{x}) - \phi_\chi(\vec{x})\right) \cdot M_\mathrm{b}, \tag{1}$$

where M_b is a binary brain mask [32], $\phi(\vec{x})$ is the unwrapped phase [33], and $\phi_\chi(\vec{x})$ is the tissue phase computed by the SHARP filter [34], which exploits the harmonicity of static magnetic fields within homogeneous media:

$$\phi_\chi(\vec{x}) = \mathrm{SHARP}\left[\phi(\vec{x})\right]. \tag{2}$$

Then, a measure of the SNLFI is provided by the local field gradient (LFG), computed according to:

$$\mathrm{LFG}(\vec{x}) = \left|\vec{\nabla}\mathrm{RPV}(\vec{x})\right|. \tag{3}$$

In the resulting LFG, which is obtained by a differential operator (namely, the gradient), some heavy border artifacts are present at the edge of the brain mask, due to the purely noisy phase (almost evenly distributed between 0 and 2π) returned by the scanner in the signal vacuum between arachnoid and dura mater and inner skull table. To get rid of the apparent SNLFI that would follow, if an arbitrary spherical structuring element $B_r[\vec{x}]$ is defined as

$$B_r[\vec{x}](\vec{y}) = \|\vec{y} - \vec{x}\| < r, \tag{4}$$

an erosion of the brain mask is obtained via a spherical structuring element $B_{r_\mathrm{e}}[0]$ centered in 0, with radius $r_\mathrm{e} \approx 4$ mm (a safe scale for complete removal of the residual extra-brain space in M_b):

$$M_\mathrm{b,e} = M_\mathrm{b} \ominus B_{r_\mathrm{e}}[0]. \tag{5}$$

Then, a regularized $\mathrm{LFG_r}$ is computed as

$$\mathrm{LFG_r}(\vec{x}) = \begin{cases} \mu_{M_\mathrm{b,e} \cap B_{r_\mathrm{d}}[\vec{x}]}\,(\mathrm{LFG}) & \text{if } \vec{x} \in M_\mathrm{b,e} \oplus B_{r_\mathrm{d}}[0]; \\ +\infty & \text{otherwise,} \end{cases} \tag{6}$$

where $r_\mathrm{d} \approx \frac{3}{2} r_\mathrm{e}$ is the dilation radius of $M_\mathrm{b,e}$ chosen to ensure that possible brain regions removed in $M_\mathrm{b,e}$ will receive a proper regularization of the Vesselness function, and the functional $\mu_{M_\mathrm{b,e} \cap B_{r_\mathrm{d}}[\vec{x}]}$, defined for any given set A as

$$\mu_A(f) = \mathrm{mean}\left(\{f(\vec{y})\,|\vec{y} \in A\}\right), \tag{7}$$

guarantees a smooth behavior of $\mathrm{LFG_r}$ based solely on LFG estimated in regions certainly belonging to the brain.

Finally, the regularization function is computed as a Fermi-Dirac distribution:

$$\mathrm{reg}(\vec{x}) = \frac{1}{1 + \exp\left[\frac{\mathrm{LFG_r}(\vec{x}) - \mu_{M_\mathrm{E}}(\mathrm{LFG_r})}{\sigma_{M_\mathrm{E}}(\mathrm{LFG_r})}\right]}, \tag{8}$$

where $M_\mathrm{E} = M_\mathrm{b} \ominus B_{r_1}[0]$ and

$$\sigma_A(f) = \mathrm{SD}\left(\{f(\vec{y})\,|\vec{y} \in A\}\right). \tag{9}$$

A choice of $r_1 \approx 20$ mm allows for the erosion of the most troublesome areas, still saving enough inner brain volume to properly estimate the moments of field gradients in regular regions.

The regularized Vesselness function is then computed as:

$$V_\mathrm{r}(\vec{x}) = V(\vec{x}) \cdot \mathrm{reg}(\vec{x}). \tag{10}$$

V_r is similar to V in regions with relatively homogeneous field, while it is reduced to nearly 0 in regions with a large $\mathrm{LFG_r}$.

B. Initial Condition

The initial condition (S_0) of MAVEN is designed in order to include large veins that may elude the local moment criteria used in the successive iterations of the algorithm (see §II-C).

Large vessels, *i.e.* vessels whose caliber is much greater than voxel size (such as – for most acquisitions – sagittal, transverse and straight sinuses, and – for high-resolution dataset – veins responsible for the drainage of both cortical and deep gray matter), have some peculiarities. Due to their size, although their magnetic susceptibility is different from their surroundings, they are characterized by a lower signal loss in SWI, because only voxels close to the vessel wall experience field inhomogeneities, resulting in the so-called ring effect [17]. As long as most internal blood voxels are considered, the fading of non-local interference from boundary voxels preserves the intravoxel phase coherence of isochromats, thus reducing the R_2^* signal loss; moreover, the higher speed of blood flow induces an apparent hyper-intensity due to the Time-of-Flight effect. As a result, in gradient echo (GRE) magnitude and SWI images, large veins may easily show a behavior that is typical of parenchyma tissues, thus eluding the segmentation criteria based on the assumption of vein hypo-intensity in SWI and high R_2^* values.

In contrast to SWI, QSM is less sensitive to smaller veins, because it is a local quantity computed by a global operator (which needs to be regularized with an unavoidable loss of spatial detail) and because of the lack of blooming effect. Conversely, it directly expresses the mean susceptibility of each voxel, and, by construction, it does not suffer from SWI and R_2^* limitations within large veins.

In order to obtain a good initial condition S_0 for the initialization of our algorithm, an approach combining Vesselness information from SWI and QSM is adopted. A modified version of QSM, $\mathrm{QSM_m}$, is computed to enhance vessel contrast relatively to other brain tissues and to reduce the influence of hyper-intense basal ganglia (BG) interface in the computation of the Vesselness map from QSM. In this respect, an initial BG mask is obtained as a global thresholding on QSM to detect substantially paramagnetic areas, according to:

$$\mathrm{BG_1}(\vec{x}) = \mathrm{QSM}(\vec{x}) > \mu_{M_\mathrm{b}}(\mathrm{QSM}) + 1.5 \cdot \sigma_{M_\mathrm{b}}(\mathrm{QSM}). \tag{11}$$

Most likely, several vessels are included within $\mathrm{BG_1}$. To get rid of possible spurious connections between large vessels and actual BG, a soft erosion is applied to $\mathrm{BG_1}$, followed by a closing to ensure a regular shape of BG:

$$\mathrm{BG_2} = (\mathrm{BG_1} \ominus B_{1\,\mathrm{mm}}[0]) \bullet B_{2\,\mathrm{mm}}[0]. \tag{12}$$

Once vessels have been disconnected from BG, a shape filter that identifies small or highly elongated structures can be safely applied to BG_2 to remove residual vessel clusters: for each 26-connected cluster (of volume $|\Omega|$ and boundary surface $|\partial\Omega|$) the compactness

$$C = |\Omega| \cdot \left(\frac{6}{|\partial\Omega|} \right)^{3/2} \tag{13}$$

and the relative anisotropy

$$\mathrm{RA} = \sqrt{\frac{1}{2}} \frac{\sqrt{(a-b)^2 + (b-c)^2 + (c-a)^2}}{a+b+c} \tag{14}$$

(a, b and c being the eigenvalues of the covariance matrix of the cluster) are computed, and BG_2 is purged of clusters with $|\Omega| < 10$ mm^3 or $C < 0.15$ or RA > 0.85.

To shave BG contrast from the QSM, an auxiliary $q(\vec{x})$ is defined as the linear interpolation of QSM on the Delaunay triangulation of a set of coats designed for each BG_2 cluster, in the outer parenchyma, as

$$\mathrm{BG_{shell}} = (\mathrm{BG_2} \oplus B_{5\,\mathrm{mm}}[0]) \backslash (\mathrm{BG_2} \oplus B_{2\,\mathrm{mm}}[0]). \tag{15}$$

The $\mathrm{QSM_m}$, specifically designed to lose sensitivity to tubular diamagnetic structures, is finally given by

$$\mathrm{QSM_m}(\vec{x}) = \begin{cases} \mathrm{QSM_{BG}}(\vec{x}) & \text{if } \mathrm{QSM_{BG}}(\vec{x}) > 0; \\ 0 & \text{otherwise,} \end{cases} \tag{16}$$

with

$$\mathrm{QSM_{BG}}(\vec{x}) = \begin{cases} q(\vec{x}) & \text{if } \vec{x} \in \mathrm{BG_2} \oplus B_{2\,\mathrm{mm}}[0]; \\ \mathrm{QSM}(\vec{x}) & \text{otherwise.} \end{cases} \tag{17}$$

Then, a regularized Vesselness function $V_{\mathrm{r,QSM}}(\vec{x})$ is computed from $\mathrm{QSM_m}$, using a Vessel Enhancing Diffusion (VED) filter (see Appendix A), tuned to detect hyper-intense vessels, *i.e.* with $\sigma \in \{i \cdot \Delta\sigma \,|\, 1 \le i \le 3\}$, and $\Delta\sigma = 0.5$ mm. $V_{\mathrm{r,QSM}}(\vec{x})$ is then combined with a Vesselness function computed from SWI, $V_{\mathrm{r,SWI}}(\vec{x})$, which detects hypo-intense vessels using $\sigma \in \{i \cdot \Delta\sigma \,|\, 1 \le i \le 10\}$ and $\Delta\sigma = 0.1$ mm, according to

$$V_{\mathrm{r,m}}(\vec{x}) = \frac{V_{\mathrm{r,QSM}}(\vec{x}) + V_{\mathrm{r,SWI}}(\vec{x})}{2}, \tag{18}$$

to equally weigh the contribution of both maps, further reducing the effect of possible residual non-vessel structures.

Finally, S_0 is computed by an hysteresis thresholding on $V_{\mathrm{r,m}}$, $V_{\mathrm{r,SWI}}$ and $V_{\mathrm{r,QSM}}$. Given two masks:

$$\begin{aligned} S_{0,\mathrm{high}}(\vec{x}) = \big\{ & \big[V_{\mathrm{r,SWI}}(\vec{x}) > \mu_{M_\mathrm{b}}(V_{\mathrm{r,SWI}}) + 4 \cdot \sigma_{M_\mathrm{b}}(V_{\mathrm{r,SWI}}) \big] \\ & \vee \big[V_{\mathrm{r,QSM}}(\vec{x}) > \mu_{M_\mathrm{b}}(V_{\mathrm{r,QSM}}) + 9 \cdot \sigma_{M_\mathrm{b}}(V_{\mathrm{r,QSM}}) \big] \big\} \\ & \wedge \vec{x} \in M_\mathrm{b}, \end{aligned} \tag{19}$$

modeled to include only voxels that definitely belong to vessel structures, and

$$S_{0,\mathrm{low}}(\vec{x}) = \big\{ V_{\mathrm{r,m}}(\vec{x}) > \mu_{M_\mathrm{b}}(V_{\mathrm{r,m}}) + 2 \cdot \sigma_{M_\mathrm{b}}(V_{\mathrm{r,m}}) \big\} \wedge \vec{x} \in M_\mathrm{b}, \tag{20}$$

which includes voxels with a moderately high value in the mean Vesselness map, the actual S_0 mask is provided by the 26-connected clusters in $S_{0,\mathrm{low}}$ that have a non-empty intersection with $S_{0,\mathrm{high}}$.

C. Iterations

Having defined the initial condition of the recursion in §II-B, the iterations are provided by the application of a spherical moving window filter: at the i-th step of the recursion, the window radius r_i is given by the i-th term of the geometric progression with initial value 20 mm and common ratio $10^{-1/2}$:

$$r_i = 20 \text{ mm} \cdot 10^{-(i-1)/2}. \tag{21}$$

For each voxel $\vec{x}$, local mean and standard deviation of SWI, Vesselness and R_2^* are calculated in the neighborhood, excluding voxels previously marked as veins. The aim is to obtain, at each iteration, adaptive thresholds that allow to identify also small vessels, which, due to partial volume effect, typically have higher SWI and lower Vesselness and R_2^* than large vessels. Each iteration refines the current estimate of $S(\vec{x})$ according to:

$$S_i(\vec{x}) = S_{i-1}(\vec{x}) \vee H(\vec{x}), \tag{22}$$

where

$$\begin{aligned} H(\vec{x}) = \; & \mathrm{SWI}(\vec{x}) < \mu_{K(\vec{x})}(\mathrm{SWI}) - 2.5 \cdot \sigma_{K(\vec{x})}(\mathrm{SWI}) \\ & \wedge V_{\mathrm{r,SWI}}(\vec{x}) > \mu_{K(\vec{x})}(V_{\mathrm{r,SWI}}) + \sigma_{K(\vec{x})}(V_{\mathrm{r,SWI}}) \\ & \wedge R_2^*(\vec{x}) > \mu_{K(\vec{x})}(R_2^*) \\ & \wedge \vec{x} \in M_\mathrm{b}, \end{aligned} \tag{23}$$

with

$$K(\vec{x}) = B_{r_i}[\vec{x}] \cap \bar{S}_{i-1} \cap M_\mathrm{b}. \tag{24}$$

The thresholds defined in Eq. 23 are closely related to those proposed in [26], provided that the Vesselness function is here computed according to a more relaxed scheme (see Appendix A) and a third condition is added on SWI.

To prevent the algorithm from emulating a kinetic process leading to the undue detection of parenchyma voxels that fall in the tails of the iteratively updated distributions (evaporation), an exit condition for the recursion is required, and it is naturally verified when the radius of the moving window filter falls below the length of the minimum voxel edge. The result of the last iteration is further refined by applying an additional condition on the size of each classified cluster, in order to reject incorrect classifications due to noise: all the detections of the vein mask are grouped in clusters of 26-connected voxels, and the clusters of cardinality lower than 3 voxels are rejected. This threshold is chosen as a compromise between obtaining a good noise suppression and avoiding the rejection of true small vein segments belonging to incompletely tracked vessels.

III. Experiment

The algorithm was tested at three different field strengths (1.5 T, 3 T and 7 T) by acquiring, at each B_0, a brain MR dataset in 4 healthy volunteers (a total of 7 males and 5 females, with median age of 29 years) who underwent examination after providing informed consent, with the approval of the Institutional Review Board. The acquired sequences were 3D double-echo spoiled GRE with a flip angle (FA) slightly higher than the parenchyma Ernst angle [26]. The

TABLE I
ACQUISITION PARAMETERS AT DIFFERENT B_0

	1.5 T	3 T	7 T
Resolution	$0.7 \times 0.7 \times 1$ mm^3	$0.5 \times 0.5 \times 1$ mm^3	$0.5 \times 0.5 \times 0.5$ mm^3
Matrix	$336 \times 336 \times 144$	$448 \times 378 \times 160$	$448 \times 448 \times 256$
FA	18°	16°	15°
T_R	36 ms	31 ms	25 ms
$T_{E,1-2}$	[9.2; 27.6] ms	[7.38; 22.14] ms	[6.12; 17.33] ms

voxel size and repetition- (T_R) and echo- ($T_{E,i}$) times were largely dependent on B_0 and were chosen to provide high SNR R_2^*-maps and images with similar susceptibility weightings in a clinically acceptable acquisition time, as reported in Table I. As a result, for each acquisition, a pair of 3D magnitude $I_{\mathrm{m},i}$ and phase ϕ_i images was available at each echo time $T_{E,i}$, $i \in \{1, 2\}$. To assess inter-scan reproducibility, one healthy control was acquired twice at 3 T, with head repositioning between the scans ($\mathrm{GRE_{pre}}$ and $\mathrm{GRE_{post}}$).

For each acquired dataset, SWI images, Vesselness maps (see Appendix A), QSM (computed by the iterative Least Square – iLSQR – algorithm described in [35]) and R_2^*-maps (see Appendix B) were derived prior to running the segmentation. All processing steps, including the MAVEN algorithm, were implemented in Matlab/C++ on a commercial workstation (Intel® Core™ i7-3820 CPU @ 3.6 GHz; RAM 16 GB) equipped with 2 GPU boards (NVIDIA GeForce® GTX 690). The whole process to obtain the segmentation starting from the double-echo GRE took 20, 30 and 60 minutes for the dataset acquired at 1.5 T, 3 T and 7 T respectively.

A. Quantitative Evaluation

The performance of MAVEN was evaluated by comparison to manual segmentation. For each segmented dataset, two minimum Intensity Projections (mIPs) of SWI and the corresponding Maximum Intensity Projections (MIPs) of QSM were selected to represent an axial slab of 20 mm at the level of BG and a sagittal slab of 10 mm on the midline, providing an adequate vein content for the following evaluations. A neuroradiologist with more than 10 years of clinical expertise segmented the veins on the mIPped SWIs, using the MIPs of QSM as additional reference. The obtained projections of manual vein segmentation were then compared with the corresponding MIPs of MAVEN, using three different geometric accuracy scores to grade the match of the 2D vein masks: the Dice Index (DI) and the Cohen's κ coefficient, which measure the overlap between two sets, and the Modified Hausdorff Distance (MHD) [36] expressed in voxel size units, which is a robust pseudo-metric on the set of segmentation masks. In order to compare the performance of MAVEN with previous methods, these scores were also computed on the results of mono/bi-parametric segmentation (m/bPS) approaches [17], [26].

The vessel density and its dependence on B_0 was then estimated by computing the length of the segmented vascular trees. First, each segmentation was skeletonized using an efficient three-dimensional parallel thinning algorithm that extracted the medial axis of the object [37], iteratively removing voxels from the volume boundary if their removal did not change the connectivity of their 26 neighborhood and if they were not endpoints. Then, the voxel skeleton was converted into a network graph described by nodes and links [38]: nodes being the voxels with more than two neighbors each; links being the groups of 26 connected voxels, with two neighbors each, connecting two nodes. This topology was finally used to calculate the network length as the sum of euclidean distances between adjacent voxels that compose the links of the graph.

To evaluate inter-scan reproducibility, the segmentations (S_{pre} and S_{post}) were computed, respectively from $\mathrm{GRE_{pre}}$ and $\mathrm{GRE_{post}}$. The second echo of $\mathrm{GRE_{post}}$ was then affine co-registered to the second echo of $\mathrm{GRE_{pre}}$ and the obtained transformation was used to map S_{post} to the S_{pre} coordinate system. The DI, κ and MHD were used to grade the matching of the co-registered vein masks.

B. Qualitative Evaluation

The previous quantitative scores convey an objective, yet coarse, measure of the geometric adherence of an estimate to a gold standard. In order to suggest a more interesting sense of the anatomical accuracy of the segmentation algorithms, a trade-off can be found between the score reproducibility and the opportunity to assign a weight to the segmentation errors according to their clinical relevance. Therefore, the same projected slabs selected for the quantitative analysis were presented in triplets (MAVEN, mPS and bPS, in random order) to two experienced neuroradiologists, not involved in the filter design, who were asked to grade, blindly and in consensus, the accuracy of the vascular tree depiction (VTD) on a 0-5 scale, compared to the corresponding mIPs of SWI and MIPs of QSM. Namely, the VTD scores correspond to:

5) optimal accuracy with possible minor misestimations of vein caliber (*i.e.* suboptimal definition of vein courses/borders);
4) moderate-to-major misestimations of vein caliber or misdetections of deep white matter (medullary) veins;
3) misdetections of cortical veins;
2) misdetections of deep gray matter veins;
1) missed detection of major venous sinuses or undue detections of non-venous midline structures (*e.g.* cerebral falx or septum pellucidum);
0) major anatomical incoherences.

C. Statistical Analysis

After testing for normality with the Kolmogorov-Smirnov tests, normally distributed scores of MAVEN versus m/bPS were compared using one-tailed t-tests for paired samples ($p_{t,\mathrm{p}}$); non parametric scores were instead compared using one-tailed Wilcoxon signed-rank test (p_{W}). Moreover, the performances of the algorithm were also compared using the corresponding parametric and non-parametric one-tailed tests for unpaired samples (*i.e.* t-test for independent samples – $p_{t,\mathrm{u}}$ – and Mann-Whitney U-test – p_U), to check whether the difference significance survived at inter-patient variability.

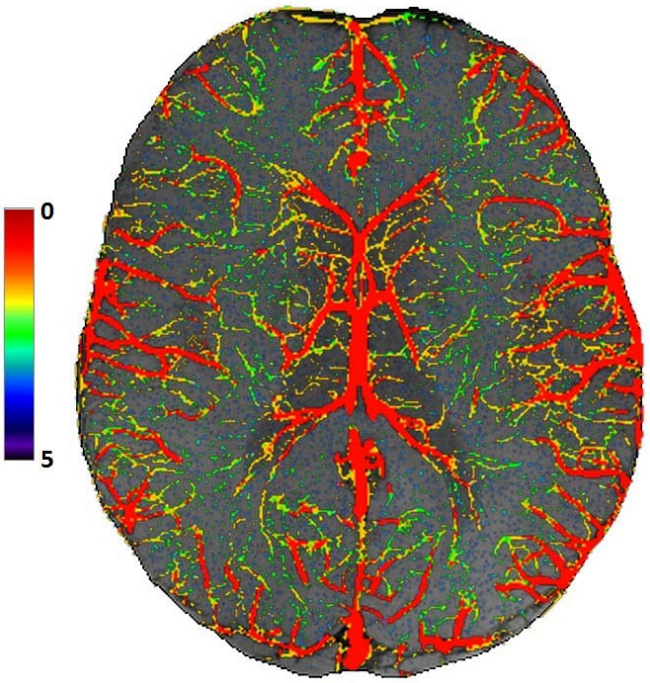

Fig. 2. Progression of MAVEN iterations on a dataset acquired at 3 T. The SWI (mIPped over 20 mm) is fused with the corresponding MIP of the result of the MAVEN segmentation before cardinality thresholding. The vein mask is represented using a look-up table that points out the voxels detected at each iteration of the algorithm (from red for the first iteration up to blue for the last one).

TABLE II
QUANTITATIVE AND QUALITATIVE COMPARISON OF SEGMENTATION METHODS

	MAVEN	mPS	bPS
DI	0.92 ± 0.03	$p_{t,\mathrm{p}} = 4.0 \cdot 10^{-13}$ 0.69 ± 0.09 $p_{t,\mathrm{u}} = 5.1 \cdot 10^{-16}$	$p_{t,\mathrm{p}} = 3.7 \cdot 10^{-16}$ 0.73 ± 0.05 $p_{t,\mathrm{u}} = 2.2 \cdot 10^{-20}$
κ	0.88 ± 0.04	$p_{t,\mathrm{p}} = 4.7.0 \cdot 10^{-15}$ 0.57 ± 0.11 $p_{t,\mathrm{u}} = 5.2 \cdot 10^{-17}$	$p_{t,\mathrm{p}} = 3.0 \cdot 10^{-18}$ 0.62 ± 0.05 $p_{t,\mathrm{u}} = 4.1 \cdot 10^{-23}$
MHD	0.30 ± 0.10	$p_{t,\mathrm{p}} = 1.5 \cdot 10^{-4}$ 1.3 ± 1.1 $p_{t,\mathrm{u}} = 5.7 \cdot 10^{-5}$	$p_{t,\mathrm{p}} = 2.4 \cdot 10^{-8}$ 0.93 ± 0.40 $p_{t,\mathrm{u}} = 7.2 \cdot 10^{-10}$
VTD	4.17 ± 0.76	$p_{\mathrm{W}} = 1.2 \cdot 10^{-5}$ 1.46 ± 0.93 $p_U = 3.0 \cdot 10^{-9}$	$p_{\mathrm{W}} = 7.7 \cdot 10^{-6}$ 2.00 ± 0.93 $p_U = 8.3 \cdot 10^{-9}$

TABLE III
MAVEN QUANTITATIVE AND QUALITATIVE ACCURACY SCORES AT DIFFERENT B_0

	1.5 T	3 T	7 T	p
DI	0.91 ± 0.02	0.92 ± 0.03	0.92 ± 0.04	0.50
κ	0.87 ± 0.03	0.88 ± 0.05	0.89 ± 0.05	0.70
MHD	0.310 ± 0.046	0.34 ± 0.10	0.25 ± 0.12	0.20
VTD	4.38 ± 0.74	4.13 ± 0.64	4.00 ± 0.93	0.62

One-way analysis of the variance – ANOVA – and Kruskal-Wallis test were used to assess differences among scores, at 1.5 T, 3 T and 7 T.

A Spearman's rank correlation test was used to verify a significant trend in the measured length of the segmented vascular trees at different B_0.

IV. RESULTS

A segmentation result obtained by the MAVEN algorithm is shown in Fig. 2, where it is pointed out how the algorithm iteratively refines the vein mask at each step. Newly detected voxels, belonging to increasingly small and tortuous vessels, are added to the large structures identified in the first iterations, thanks to the adaptive and local thresholds computed excluding voxels previously marked as veins. The MAVEN performance against manual segmentation is compared with m/bPS performances in Table II, where the mean and standard deviation of each score are reported along with the significance level p of the differences between previous methods and MAVEN. DI, κ and MHD consistently show that MAVEN better matches the actual gold standard (manual segmentation) than m/bPS. The higher accuracy in the MAVEN venous tree depiction is also confirmed by the qualitative evaluation. Interestingly, the statistical significance observed at paired t- and Wilcoxon tests survives even at the independent t- and U-tests, showing that the observed performance differences go beyond the possible inter-patient variability of the venous tree. An illustrative segmentation result is shown in Fig. 3, where the MAVEN classification is placed side by side with the results of m/bPS and the manual segmentation as reference in the axial and sagittal slabs of a sample dataset, pointing out how MAVEN outperforms previous methods both in terms of false positives and false negatives. An additional result is exemplified in Fig. 4 to demonstrate that the MAVEN algorithm is capable to correctly classify veins at different axial levels of the brain, neglecting hypo-intensities that are mainly due to artifacts.

The segmentation results obtained at 1.5, 3 and 7 T are shown in Fig. 5, Fig. 6 and Fig. 7, respectively, where the MAVEN results are displayed together with the corresponding SWI and their fusion. The MAVEN accuracy scores grouped by B_0 are shown in Table III, where the mean and standard deviation of each score are reported, along with the significance level p of the differences among groups. Though the measured length of the segmented vascular trees ([14.8±1.5] m at 1.5 T, [21.3±3.0] m at 3 T and [28.5±5.6] m at 7 T, respectively) reflects a visible vein density increase with the B_0 (trend confirmed by the Spearman's rank correlation test: $r_s = 0.91$; $p = 2.8 \cdot 10^{-5}$), the scores in Table III are not significantly different. This shows that venous tree segmentation by MAVEN is feasible at several field strengths, with no need of algorithm parameter adjustments or human interaction, thanks to the intrinsically adaptive thresholds used.

The comparison of S_{pre} and S_{post} shows a good overlap (also visible in Fig. 8), with DI = 0.67, $\kappa = 0.66$ and MHD = 0.52.

V. DISCUSSION

In this work, a fully automated method based on structural, morphological and relaxometric information has been

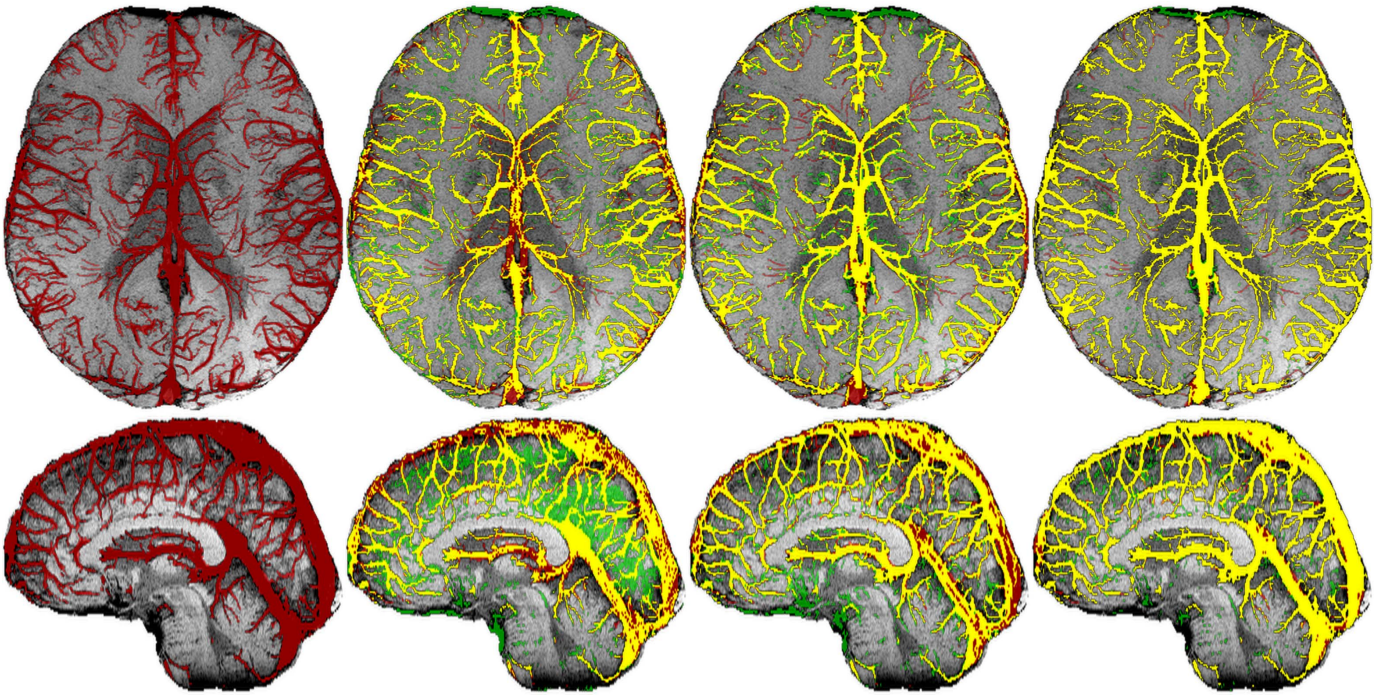

Fig. 3. RGB color-coded fusion of manual segmentation (red) and automated segmentation methods (green, from the second to the fourth column: mPS, bPS and MAVEN) from a brain dataset acquired at 3 T. All segmentations are MIPped and fused with SWI-mIP: image projections cover 20 mm in the axial slabs (first row) and 10 mm in the sagittal slabs (second row). From the second to the fourth column: yellow voxels correspond to true positives; green voxels correspond to false positives; red voxels correspond to false negatives. The lower incidence of green and red areas in the fourth column indicates that MAVEN better matches manual segmentation in comparison to mPS and bPS, which frequently barely detect some thin vessels and large caliber veins, and wrongly classify as vein several fibrous structures in the midline and susceptibility artifacts near the bone interfaces.

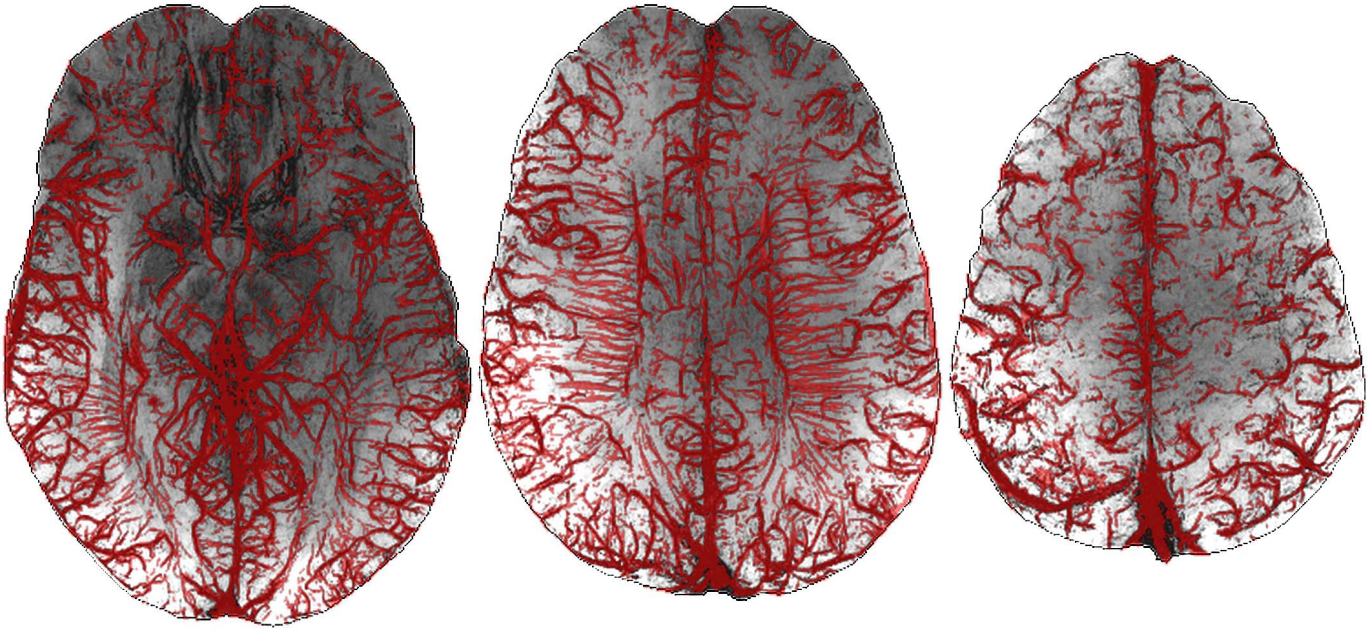

Fig. 4. Segmentation results at different axial levels of the brain at 7 T (fusion of SWI-mIP with MAVEN-MIP over 20 mm). MAVEN is able to reject artifacts due to SNLFI without losing sensitivity in vein detection (left), it exhibits a high accuracy in detection of cortical and deep white matter veins (center) and correctly segments superior sagittal sinus and superficial veins (right).

proposed, in order to segment the entire cerebral venous system. The proposed approach takes into account several key points that are not addressed by previous methods, leading to an accurate segmentation of the venous tree, which combines a reduction of false positives with an improved detection of true positives when compared to m/bPS.

The greater accuracy in vessel display achieved by MAVEN seems partially due to the lack of a comprehensive vein

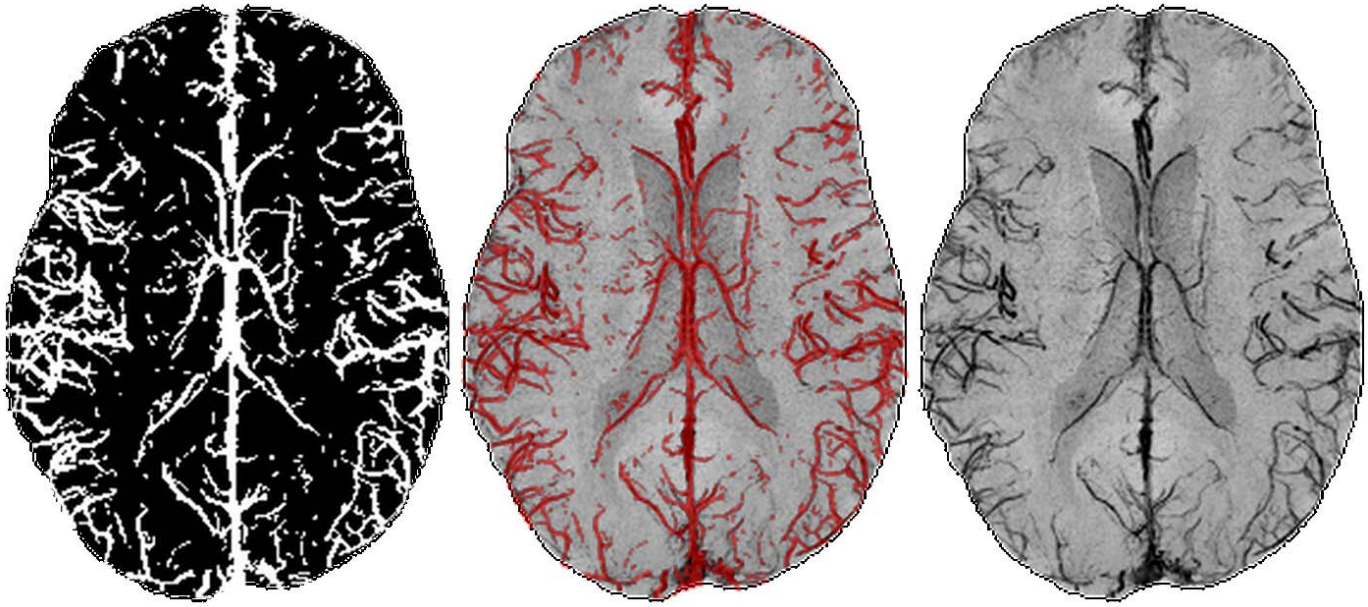

Fig. 5. Segmentation result at 1.5 T. From left to right: MAVEN-MIP; fusion of SWI-mIP with MAVEN-MIP; SWI-mIP. Image projections cover 20 mm in the head-foot direction.

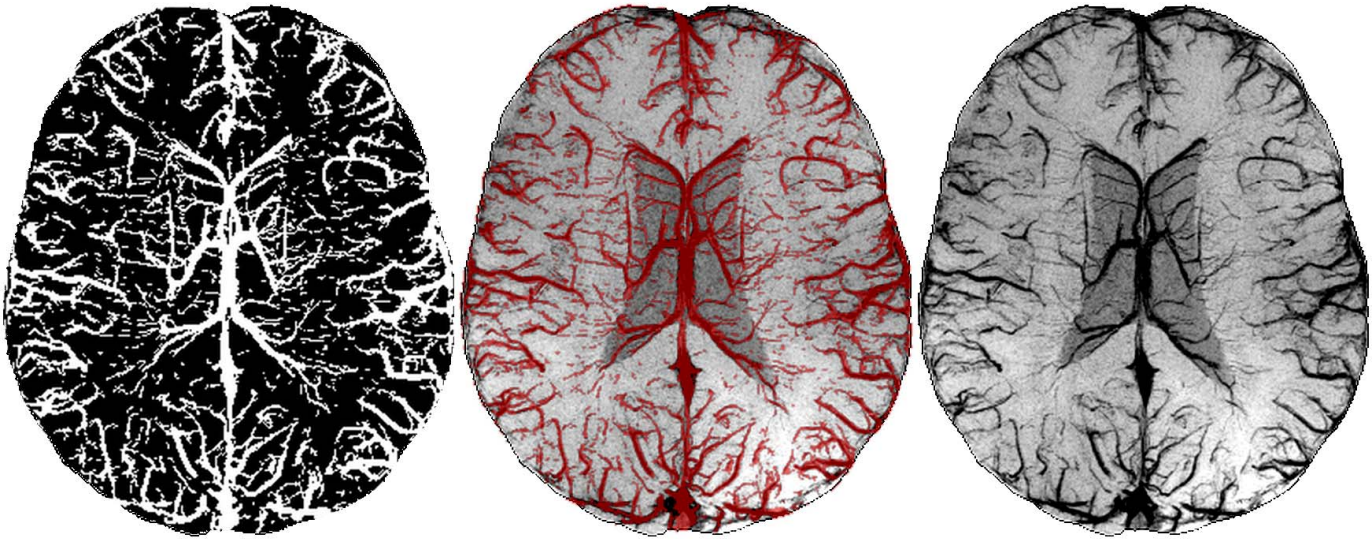

Fig. 6. Segmentation result at 3 T. From left to right: MAVEN-MIP; fusion of SWI-mIP with MAVEN-MIP; SWI-mIP. Image projections cover 20 mm in the head-foot direction.

characterization (morphologic, structural and relaxometric) in the other approaches. Indeed, each independent criterion used in MAVEN brings its intrinsic added value to the final segmentation result. Compared to mPS, the use of a relaxometric reference helps to avoid incorrect classification of elongated hypo-intense structures – such as cerebral sulci, whose intensity resembles the venous one in SWI images when FA increases. Similarly, the Vesselness map limits the detection to tubular structures only, thus reducing misclassification in the mid-sagittal plane, in BG and in parenchyma voxels, adjacent to veins, that may undergo evaporation in the monoparametric iterative process based on SWI images only, leading to vein caliber misestimations. On the other hand, the use of structural information (SWI), which is not considered in bPS, increases the algorithm sensitivity to small veins, such as deep white matter veins, and, used together with the other criteria, makes it possible to adopt less restrictive threshold values, leading to an improved detection of true positives without loss of specificity. In addition, MAVEN incorporates a preliminary regularization step on the Vesselness functions: this solution modifies the Vesselness values, making the algorithm less sensitive at the level of the roof of the petrous bones, in the fronto-basal midline region and in the interhemispheric fissure, where SNLFI induce susceptibility artifacts not related to tissue properties. As a result, incorrect classifications of voxels that resemble venous signal intensity

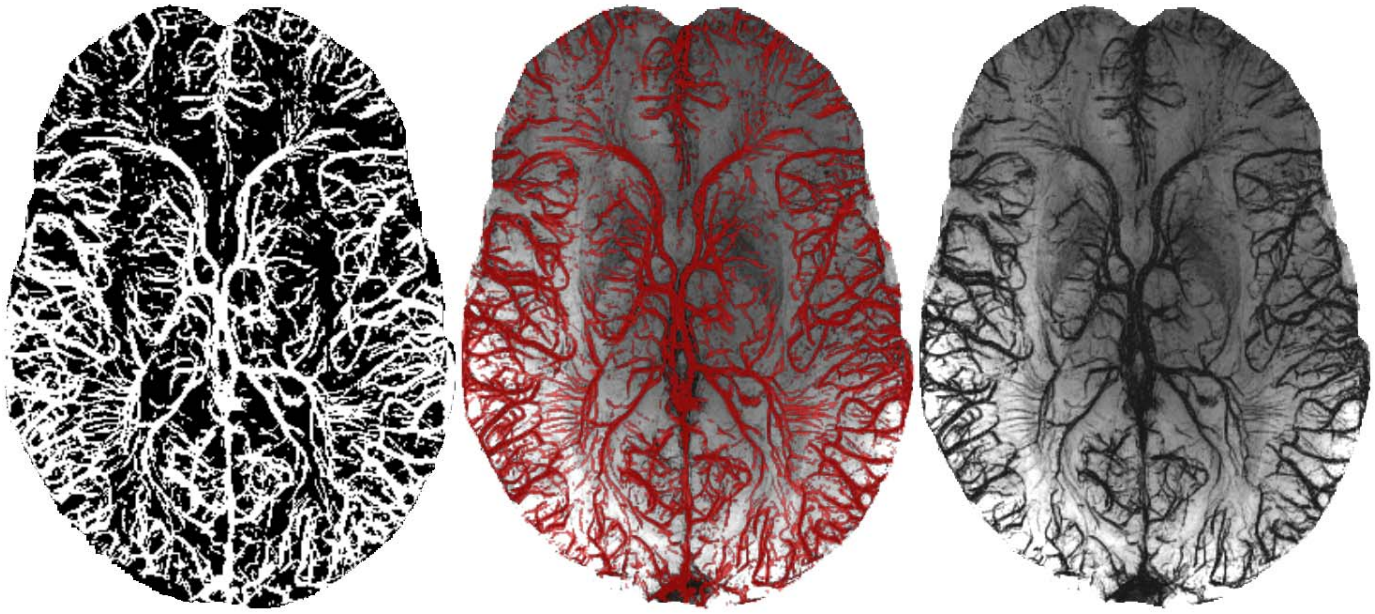

Fig. 7. Segmentation result at 7 T. From left to right: MAVEN-MIP; fusion of SWI-mIP with MAVEN-MIP; SWI-mIP. Image projections cover 20 mm in the head-foot direction.

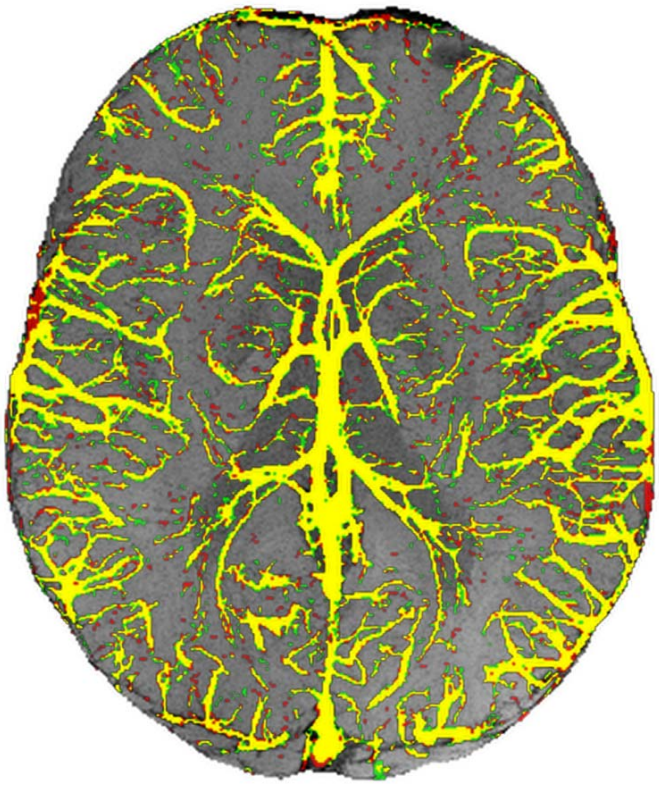

Fig. 8. RGB color-coded fusion of S_{pre} (red) and S_{post} (green) maps, MIPped over 20 mm in the head-foot direction, superimposed on the SWI reference. Yellow areas correspond to matched vein detections.

are strongly reduced by MAVEN in SNLFI regions, where the accuracy of m/bPS segmentation is instead degraded by the large amount of false positives. Moreover, regarding the detection of large vessels (*e.g.* sagittal sinus and superficial veins), the typical problems of segmentation methods based on the local moments of signal intensity are bypassed by the MAVEN initial condition, thanks to a combination of morphological information extracted from SWI and QSM. This leads to a further reduction of false negatives in MAVEN (compared to m/bPS) that, consequently, shows a good overlap with manual segmentation. The use of QSM in the design of the initial condition also makes the algorithm less sensitive to vessel directionality relative to $\vec{B}_0$. Indeed, the venous blood phase depends on the vessel orientation relative to the main magnetic field, causing a variable appearance of otherwise similar venous vessels in SWI. As long as a vessel remains visible in SWI images, this effect is partially compensated throughout the MAVEN routine by the use of multi-parametric thresholds, iteratively computed on local moving windows. Even if the vessel visibility is compromised, its detectability is fostered anyway in the initial step by the QSM, which is independent on vessel orientation [39].

The venous tree segmentation by MAVEN proves to be feasible at 1.5 T, 3 T and 7 T with comparable accuracy scores. However, it should be kept in mind that, when segmenting datasets acquired at the different field strengths, the variation of both physical conditions and acquisition parameters affects the vein visibility. In particular, a higher field strength provides higher SNR and increases vessel contrast in a reasonable acquisition time; a higher scan resolution allows to visualize smaller structures; anisotropic voxels (usually with the slice thickness two or four times larger than the in-plane grid element sizes), compared to isotropic voxels with the same in-plane dimensions, guarantee, in SWI images, a better visibility of vessels with caliber comparable to the in-plane resolution [40], but they provide enlarged vessel size in the through-plane direction. Taking all these factors into account, the used acquisition parameters lead to an increase of visible vein density with B_0, due to enhanced resolution and higher susceptibility contrast, and this is reflected in the segmentation results. This trend is proven by the increasing lengths of the

segmented vascular trees with the B_0, and it is also clearly visible in Fig. 5, Fig. 6 and Fig. 7.

Of note, the vein visibility also affects the minimum diameter of vessels that MAVEN can accurately segment. Indeed, due to the blooming artifact, even veins that are smaller than the voxel size leave a clear sign within SWI [17], and they can thus be detected by our algorithm. This effect, actually dependent on voxel aspect ratio, increases at higher field strengths, lower local oxygen saturation levels and longer T_Es, allowing to detect vessels up to four times smaller than the voxel itself in standard unenhanced clinical acquisitions.

The presented algorithm, when applied to repeated acquisitions of the same subject, leads to a MHD between the two segmentations well below 1 (*i.e.* the resolution of the used dataset), thus indicating an excellent inter-scan reproducibility at 3 T.

MAVEN, therefore, offers a reproducible, accurate and completely automated method for vein detection that provides trustworthy segmentations on a large spectrum of acquired datasets.

We are aware that the presented algorithm is not without limitations. First, it is based on the assumption that only venous blood susceptibility can lead a vessel voxel to show low SWI- and high R_2^*-values. However, possible non compensated flows in GRE acquisitions might give rise to signal loss in large arterial vessels that, consequently, resemble veins in shape and SWI- and R_2^*-values, and may thus be incorrectly mistaken for veins by MAVEN. Second, MAVEN takes advantage of the R_2^* map, whose computation requires a double (or multi) echo acquisition. Of note, in this work a double echo acquisition and, consequently, the assumption of a monoexponential FID for the brain tissues are used: those choices are motivated by the fact that in MAVEN it is preferable to obtain a high SNR SWI (*i.e.* an echo acquired with an adequately low bandwidth) than a more accurate R_2^* mapping, since the vein R_2^* estimates are merely used to better distinguish between false and true positives in the multi-parametric thresholding. Though, in principle, no extra acquisition time is typically necessary for the additional low T_E image of this dual echo configuration, as it fits within an otherwise sequence dead-time, the need for a second echo could rule out the method in retrospective studies based on single-echo GREs. However, a MAVEN variant that substitutes R_2^* information with other tissue properties could be explored in future works, extending the scope of the algorithm to any GRE acquisition.

Despite the apparently large number of free algorithm parameters, their actual values have been set up largely according to geometrical and tissue evaluations on the anatomical structures at issue. Most importantly, it has been observed that even moderate variations of the values – compatibly with the above evaluations – only lead to negligible effects on the results.

It seems desirable to integrate MAVEN in a tubular tracking-based approach, as the one described in [30], to obtain a comprehensive framework for morphological analysis of the whole-brain venous tree, including, but not limited to, the measurements of length, curvature and caliber of each vein.

Moreover, since a vein mask is needed to compute oxygen extraction fraction (OEF) maps from MR phase images, an accurate and automated algorithm for 3D segmentation of the vessel tree of the whole brain represents an essential method for an OEF quantification tool. This would in fact minimize typical issues encountered in this calculation, such as the spatial resolution limited by the amount of venous pixels detected, and the exclusion of slices at BG level to avoid susceptibility effects of iron deposition [41].

Conversely, the use of the 3D vein mask would also be valuable in a complementary way: knowing their exact location, vein voxels could be proficiently and automatically excluded from parenchymal ROIs when measuring quantitative parameters. In fact, despite the relative small vein volume, their inclusion may cause severe biases, since even small amounts of paramagnetic veins may greatly alter the measure of mean magnetic susceptibility in a white matter region.

Besides, the accurate definition of the venous intracranial compartment may find useful applications in the study of other fluid networks, such as the CSF and the recently described cerebral lymphatic system [42]. In particular, it could be hypothesized that, even if the scales involved in the lymphatic network do not allow for a direct MRI investigation, a detailed knowledge of the venous morphology may provide the definition of realistic compartments and boundary conditions for phenomenological hydrodynamics simulations of the biological fluid interaction [43].

In conclusion, MAVEN represents an automated algorithm for the brain vein segmentation, offering an accurate and reproducible method that could provide quantitative measurements in future studies of different clinical conditions, ranging from traumatic brain injuries to neurodegenerative or neurovascular disorders.

Appendix A Vesselness

The Vesselness $V(\vec{x})$ is a likeliness function that distinguishes tubular structures (veins) from non-tubular or different-contrast features.

For a given dataset $\mathcal{F}(\vec{x})$, the non-smoothed Vesselness $\mathcal{V}(\vec{x})$ is traditionally computed by adopting a multi-scale approach in order to identify vessels of different caliber [22]. $\mathcal{F}$ is preliminarily filtered by Gaussian kernels with different standard deviations σ, corresponding to the different spatial scales. For each scale and each voxel, the local second-order pattern is examined using the Hessian tensor $\mathbf{H}_\sigma(\vec{x})$ and its eigenvalues, sorted by increasing magnitude ($|\lambda_{\sigma,1}(\vec{x})| < |\lambda_{\sigma,2}(\vec{x})| < |\lambda_{\sigma,3}(\vec{x})|$). If the vessels are expected to be dark within $\mathcal{F}$ (*e.g.* in SWI), since low-signal tubular structures are characterized by high values of λ_2 and λ_3, the Vesselness measure at each scale is calculated as:

$$\mathcal{V}_\sigma[\mathcal{F}](\vec{x}) = \begin{cases} 0 & \text{if } \lambda_{\sigma,2}(\vec{x}) < 0 \vee \lambda_{\sigma,3}(\vec{x}) < 0, \\ \left(1 + e^{\frac{-A_\sigma(\vec{x})^2}{2\alpha^2}}\right) e^{\frac{-B_\sigma(\vec{x})^2}{2\beta^2}} \left(1 + e^{\frac{-S_\sigma(\vec{x})^2}{2\gamma_\sigma^2}}\right) & \\ \quad \text{otherwise,} & \end{cases} \tag{25}$$

where

$$A_\sigma(\vec{x}) \equiv \frac{|\lambda_{\sigma,2}(\vec{x})|}{|\lambda_{\sigma,3}(\vec{x})|} \tag{26}$$

is essential for distinguishing plate-like from linear structures,

$$B_\sigma(\vec{x}) \equiv \frac{|\lambda_{\sigma,1}(\vec{x})|}{\sqrt{|\lambda_{\sigma,2}(\vec{x})\lambda_{\sigma,3}(\vec{x})|}} \tag{27}$$

accounts for the deviation from a blob-like structure, and

$$S_\sigma(\vec{x}) \equiv \sqrt{\lambda_{\sigma,1}(\vec{x})^2 + \lambda_{\sigma,2}(\vec{x})^2 + \lambda_{\sigma,3}(\vec{x})^2} \tag{28}$$

allows for tuning the result as a function of the background noise. In case of bright vessels (*e.g.* in QSM), Eq. 25 becomes:

$$\mathcal{V}_\sigma[\mathcal{F}](\vec{x}) = \begin{cases} 0 \quad \text{if } \lambda_{\sigma,2}(\vec{x}) > 0 \vee \lambda_{\sigma,3}(\vec{x}) > 0, \\ \left(1 + e^{\frac{-A_\sigma(\vec{x})^2}{2\alpha^2}}\right) e^{\frac{-B_\sigma(\vec{x})^2}{2\beta^2}} \left(1 + e^{\frac{-S_\sigma(\vec{x})^2}{2\gamma_\sigma^2}}\right) \\ \quad \text{otherwise.} \end{cases} \tag{29}$$

In the MAVEN setup, the tuning parameters α and β were set to 0.5, according to [24], whereas

$$\gamma_\sigma = \frac{1}{2} \max_{\vec{x}} \|\mathbf{H}_\sigma(\vec{x})\|_F \,. \tag{30}$$

For each voxel, $\vec{x}$, $\mathcal{V}$ is finally computed as:

$$\mathcal{V}[\mathcal{F}](\vec{x}) = \max_\sigma \mathcal{V}_\sigma[\mathcal{F}](\vec{x}). \tag{31}$$

In order to obtain the actual Vesselness V from the dataset $\mathcal{F}$, a rotationally invariant version of the Vessel Enhancing Diffusion filter (VED) [26] is applied to $\mathcal{F}$. In particular, the above definition of the $\mathcal{V}$ measure allows for evolving $\mathcal{F}$ according to a scheme of anisotropic diffusion, highly restricted when perpendicular to tubular structures [23]:

$$\begin{cases} \frac{\partial}{\partial t} F(\vec{x}, t) = \vec{\nabla} \cdot \left\{ \mathbf{D}[F(\cdot, t)](\vec{x}) \cdot \vec{\nabla} F(\vec{x}, t) \right\}; \\ F(\vec{x}, 0) = \mathcal{F}(\vec{x}), \end{cases} \tag{32}$$

where

$$\begin{aligned} &\mathbf{D}[F(\cdot, t)](\vec{x}) \\ &\quad \equiv \mathbf{Q}[F(\cdot, t)](\vec{x}) \cdot \mathbf{\Lambda}[F(\cdot, t)](\vec{x}) \cdot \mathbf{Q}[F(\cdot, t)](\vec{x})^T, \end{aligned} \tag{33}$$

$$\begin{aligned} &\mathbf{\Lambda}[F(\cdot, t)](\vec{x}) \\ &\quad \equiv \mathbb{1} + \mathcal{V}[F(\cdot, t)](\vec{x})^{1/s} \cdot \left[\text{diag}(\omega, \epsilon, \epsilon) - \mathbb{1}\right], \end{aligned} \tag{34}$$

$\mathbf{Q}[F(\cdot, t)](\vec{x})$ is the matrix of the $\mathbf{H}_\sigma(\vec{x})$ eigenvectors at the scale σ with the maximum $\mathcal{V}_\sigma[F(\cdot, t)](\vec{x})$ response, ω is the strenght of anisotropic diffusion, s the sensitivity to the Vesselness response, and ϵ ensures the positive definiteness of the tensor. Note that $\mathbf{D}$ is continuously updated by a new calculation of $\mathcal{V}$ on the evolved F. The actual Vesselness V from the dataset $\mathcal{F}$ is then obtained as:

$$V[\mathcal{F}](\vec{x}) = \mathcal{V}[F(\cdot, t_e)](\vec{x}). \tag{35}$$

To improve the VED filtering and obtain a high-SNR continuous 3D model of the veins, in the MAVEN setup $\omega = 25$, $\epsilon = 10^{-2}$, the sensitivity $s = 3$ and the diffusion time t_e was set to 0.4.

Appendix B
R_2^* Map Calculation

The acquired datasets were first processed in order to enhance the Signal-to-Noise Ratio (SNR) of the original images to be used for R_2^*-map extraction. For this purpose, a modified version of the Non Local Means (NLM) approach [44], developed for parallel MRI acquisitions with noise power spatially varying (SVN-NLM) within the Field of View (FOV) [45], was adapted for multi-component 3D datasets.

As described in [46], the phase images ϕ_i corresponding to each acquired echo were first high-pass filtered to remove unwanted low-frequency B_0 variations due to exogenous contrast mechanisms (e.g. shimming problems, imperfect phase refocusing of spatially selective Radio-Frequency (RF) pulses, complex coil sensitivity, etc.). Each pair of magnitude ($I_{\text{m},i}$) and phase ($\phi_{\text{hp},i}$) images was then converted in the real/imaginary representation of the complex domain ($I_{\text{R},i}$ and $I_{\text{I},i}$). These four 3D images were considered as a discrete version of a general multi-component image $X : \mathbb{R}^N \to \mathbb{R}^M$ ($N = 3$ and $M = 4$) with a bounded support $\Omega \subset \mathbb{R}^N$, and thus processed via SVN-MNLM according to [47]. Due to the high computational complexity of the scheme, a multi-GPU implementation of the algorithm [48] was used.

The denoised $\tilde{I}_{\text{R},i}$ and $\tilde{I}_{\text{I},i}$ were then combined to obtain the magnitude images for each echo:

$$\tilde{I}_{\text{m},i} = \sqrt{\tilde{I}_{\text{R},i}^2 + \tilde{I}_{\text{I},i}^2}, \tag{36}$$

whence the R_2^*-map was derived as

$$R_2^* = \frac{\log\left(\tilde{I}_{\text{m},1} / \tilde{I}_{\text{m},2}\right)}{T_{E,2} - T_{E,1}}. \tag{37}$$

Acknowledgment

Mario Magliulo and Massimiliano Sorbillo are gratefully acknowledged for their valuable IT assistance.

References

[1] E. M. Haacke, Y. Xu, Y.-C. N. Cheng, and J. R. Reichenbach, "Susceptibility weighted imaging (SWI)," *Magn. Reson. Med.*, vol. 52, no. 3, pp. 612–618, Sep. 2004.

[2] J. M. Coutinho, J. J. Gerritsma, S. M. Zuurbier, and J. Stam, "Isolated cortical vein thrombosis: Systematic review of case reports and case series," *Stroke*, vol. 45, no. 6, pp. 1836–1838, 2014.

[3] S. Chen *et al.*, "Venous system in acute brain injury: Mechanisms of pathophysiological change and function," *Exp. Neurol.*, vol. 272, pp. 4–10, Oct. 2015.

[4] E. F. Toro, "Brain venous haemodynamics, neurological diseases and mathematical modelling. A review," *Appl. Math. Comput.*, vol. 272, pp. 542–579, Jan. 2016.

[5] C. B. Beggs, "Venous hemodynamics in neurological disorders: An analytical review with hydrodynamic analysis," *BMC Med.*, vol. 11, no. 1, p. 142, 2013.

[6] C. W. Adams, Y. H. Abdulla, E. M. Torres, and R. N. Poston, "Periventricular lesions in multiple sclerosis: Their perivenous origin and relationship to granular ependymitis," *Neuropathol. Appl. Neurobiol.*, vol. 13, no. 2, pp. 141–152, 1987.

[7] R. De Simone, A. Ranieri, S. Montella, M. Marchese, and V. Bonavita, "Sinus venous stenosis–associated idiopathic intracranial hypertension without papilledema as a powerful risk factor for progression and refractoriness of headache," *Current Pain Headache Rep.*, vol. 16, no. 3, pp. 261–269, Jun. 2012.

[8] G. Saposnik *et al.*, "Diagnosis and management of cerebral venous thrombosis: A statement for healthcare professionals from the american heart association/american stroke association," *Stroke*, vol. 48, no. 2, pp. 1158–1192, 2011.

[9] F. Y. Tsai, V. Kostanian, M. Rivera, K.-W. Lee, C. C. Chen, and T. H. Nguyen, "Cerebral venous congestion as indication for thrombolytic treatment," *CardioVascular Intervent. Radiol.*, vol. 30, no. 4, pp. 675–687, Jul. 2007.

[10] W. R. Brown and C. R. Thore, "Review: Cerebral microvascular pathology in ageing and neurodegeneration," *Neuropathol. Appl. Neurobiol.*, vol. 37, no. 1, pp. 56–74, Feb. 2011.

[11] G. Bateman, "The pathophysiology of idiopathic normal pressure hydrocephalus: Cerebral ischemia or altered venous hemodynamics?" *AJNR Amer. J. Neuroradiol.*, vol. 29, no. 1, pp. 198–203, 2008.

[12] S. Yan *et al.*, "Increased visibility of deep medullary veins in leukoaraiosis: A 3-T MRI study," *Front Aging Neurosci.*, vol. 6, p. 144, Sep. 2014.

[13] D. M. Moody, W. R. Brown, V. R. Challa, and R. L. Anderson, "Periventricular venous collagenosis: Association with leukoaraiosis," *Radiol.*, vol. 194, no. 2, pp. 469–476, 1995.

[14] T. Kau *et al.*, "The 'central vein sign': Is there a place for susceptibility weighted imaging in possible multiple sclerosis?" *Eur. Radiol.*, vol. 23, no. 7, pp. 1956–1962, Jul. 2013.

[15] M. I. Gaitán, M. P. de Alwis, P. Sati, G. Nair, and D. S. Reich, "Multiple sclerosis shrinks intralesional, and enlarges extralesional, brain parenchymal veins," *Neurology*, vol. 80, no. 2, pp. 145–151, 2013.

[16] R. Zivadinov *et al.*, "Decreased brain venous vasculature visibility on susceptibility-weighted imaging venography in patients with multiple sclerosis is related to chronic cerebrospinal venous insufficiency," *BMC Neurol.*, vol. 11, no. 1, p. 1, 2011.

[17] E. M. Haacke and J. R. Reichenbach, *Susceptibility Weighted Imaging MRI: Basic Concepts and Clinical Applications*. Hoboken, NJ, USA: Wiley, 2014.

[18] F. Arrigoni *et al.*, "Deep medullary vein involvement in neonates with brain damage: An MR imaging study," *AJNR Amer. J. Neuroradiol.*, vol. 32, no. 11, pp. 2030–2036, 2011.

[19] S. Bériault, A. F. Sadikot, F. Alsubaie, S. Drouin, D. L. Collins, and G. B. Pike, "Neuronavigation using susceptibility-weighted venography: Application to deep brain stimulation and comparison with gadolinium contrast: Technical note," *J. Neurosurgery*, vol. 121, no. 1, pp. 131–141, 2014.

[20] W. L. Nowinski, I. Volkau, Y. Marchenko, A. Thirunavuukarasuu, T. T. Ng, and V. M. Runge, "A 3D model of human cerebrovasculature derived from 3T magnetic resonance angiography," *Neuroinformatics*, vol. 7, no. 1, pp. 23–36, 2009.

[21] D. Lesage, E. D. Angelini, I. Bloch, and G. Funka-Lea, "A review of 3D vessel lumen segmentation techniques: Models, features and extraction schemes," *Med. Image Anal.*, vol. 13, no. 6, pp. 819–845, Aug. 2009.

[22] A. F. Frangi, W. J. Niessen, K. L. Vincken, and M. A. Viergever, "Multiscale vessel enhancement filtering," in *Proc. MICCAI*, 1998, pp. 130–137.

[23] R. Manniesing, M. A. Viergever, and W. J. Niessen, "Vessel enhancing diffusion: A scale space representation of vessel structures," *Med. Image Anal.*, vol. 10, no. 6, pp. 815–825, 2006.

[24] P. J. Koopmans, R. Manniesing, W. J. Niessen, M. A. Viergever, and M. Barth, "MR venography of the human brain using susceptibility weighted imaging at very high field strength," *Magn. Reson. Mater. Phys., Biol. Med.*, vol. 21, no. 1, pp. 149–158, 2008.

[25] S. Bériault, M. Archambault-Wallenburg, A. F. Sadikot, D. L. Collins, and G. B. Pike, "Automatic Markov random field segmentation of susceptibility-weighted MR venography," in *Clinical Image-Based Procedures. Translational Research in Medical Imaging*. Cham, Switzerland: Springer, 2014, pp. 39–47.

[26] S. Monti *et al.*, "A multiparametric and multiscale approach to automated segmentation of brain veins," in *Proc. 37th Annu. Int. Conf. IEEE Eng. Med. Biol. Soc. (EMBC)*, Aug. 2015, pp. 3041–3044.

[27] S. Bériault, Y. Xiao, D. L. Collins, and G. B. Pike, "Automatic SWI venography segmentation using conditional random fields," *IEEE Trans. Med. Imag.*, vol. 34, no. 12, pp. 2478–2491, Dec. 2015.

[28] X. Xu *et al.*, "Segmentation of cerebral venous vessel in SWI based on multi-adaptive threshold with vessel enhancement and background effects elimination," in *Proc. 6th Int. Conf. Internet Comput. Sci. Eng. (ICICSE)*, Apr. 2012, pp. 107–111.

[29] H. J. Kuijf, W. H. Bouvy, J. J. M. Zwanenburg, M. A. Viergever, G. J. Biessels, and K. L. Vincken, "Automated detection of periventricular veins on 7 T brain MRI," *Proc. SPIE*, vol. 9413, p. 94132T, 2015.

[30] H. J. Kuijf *et al.*, "Quantification of deep medullary veins at 7 T brain MRI," *Eur. Radiol.*, vol. 26, no. 10, pp. 3412–3418, Oct. 2016.

[31] S. Monti *et al.*, "Automated multi-parametric segmentation of brain veins from GRE acquisition," in *Proc. Int. Soc. Mag. Reson. Med.*, 2016, p. 1906.

[32] S. M. Smith, "Fast robust automated brain extraction," *Human Brain Mapping*, vol. 17, no. 3, pp. 143–155, 2002.

[33] R. Cusack and N. Papadakis, "New robust 3-D phase unwrapping algorithms: Application to magnetic field mapping and undistorting echoplanar images," *NeuroImage*, vol. 16, no. 3, pp. 754–764, Jul. 2002.

[34] F. Schweser, A. Deistung, B. W. Lehr, and J. R. Reichenbach, "Quantitative imaging of intrinsic magnetic tissue properties using MRI signal phase: An approach to *in vivo* brain iron metabolism?" *NeuroImage*, vol. 54, no. 4, pp. 2789–2807, Feb. 2011.

[35] W. Li *et al.*, "A method for estimating and removing streaking artifacts in quantitative susceptibility mapping," *NeuroImage*, vol. 108, pp. 111–122, Mar. 2015.

[36] M.-P. Dubuisson and A. K. Jain, "A modified Hausdorff distance for object matching," in *Proc. 12th IAPR Int. Conf. Pattern Recognit. (ICPR)*, vol. 1. Oct. 1994, pp. 566–568.

[37] T. C. Lee, R. L. Kashyap, and C. N. Chu, "Building skeleton models via 3-D medial surface axis thinning algorithms," *CVGIP, Graph. Models Image Process.*, vol. 56, no. 6, pp. 462–478, 1994.

[38] M. Kerschnitzki *et al.*, "Architecture of the osteocyte network correlates with bone material quality," *J. Bone Mineral Res.*, vol. 28, no. 8, pp. 1837–1845, 2013.

[39] E. M. Haacke, J. Tang, J. Neelavalli, and Y. C. N. Cheng, "Susceptibility mapping as a means to visualize veins and quantify oxygen saturation," *J. Magn. Reson. Imag.*, vol. 32, no. 3, pp. 663–676, Sep. 2010.

[40] Y. Xu and E. M. Haacke, "The role of voxel aspect ratio in determining apparent vascular phase behavior in susceptibility weighted imaging," *Magn. Reson. Imag.*, vol. 24, no. 2, pp. 155–160, Feb. 2006.

[41] K. Kudo *et al.*, "Oxygen extraction fraction measurement using quantitative susceptibility mapping: Comparison with positron emission tomography," *J. Cerebral Blood Flow Metabolism*, vol. 36, no. 8, p. 0271678X15606713, 2015.

[42] A. Louveau *et al.*, "Structural and functional features of central nervous system lymphatic vessels," *Nature*, vol. 523, no. 7560, pp. 337–341, 2015.

[43] L. O. Müller and E. F. Toro, "A global multiscale mathematical model for the human circulation with emphasis on the venous system," *Int. J. Numer. Methods Biomed. Eng.*, vol. 30, no. 7, pp. 681–725, Jul. 2014.

[44] A. Buades, B. Coll, and J.-M. Morel, "A review of image denoising algorithms, with a new one," *Multiscale Model. Simul.*, vol. 4, no. 2, pp. 490–530, 2005.

[45] P. Borrelli, G. Palma, M. Comerci, and B. Alfano, "Unbiased noise estimation and denoising in parallel magnetic resonance imaging," in *Proc. IEEE Int. Conf. Acoust., Speech Signal Process. (ICASSP)*, May 2014, pp. 1230–1234.

[46] P. Borrelli *et al.*, "Improving signal-to-noise ratio in susceptibility weighted imaging: A novel multicomponent non-local approach," *PLoS ONE*, vol. 10, no. 6, p. e0126835, 2015.

[47] G. Palma *et al.*, "A novel multiparametric approach to 3D quantitative MRI of the brain," *PLoS ONE*, vol. 10, no. 8, p. e0134963, 2015.

[48] G. Palma *et al.*, "3D non-local means denoising via multi-GPU," in *Proc. Federated Conf. Comput. Sci. Inf. Syst. (FedCSIS)*, Sep. 2013, pp. 495–498.